Meteoritics & Planetary Science 55, Nr 4, 818–831 (2020)
doi: 10.1111/maps.13466-3270

^{53}Mn and ^{60}Fe in iron meteorites—New data and model calculations

Ingo LEYA[1*], Jean-Christophe DAVID[2], Thomas FAESTERMANN[3], Michaela FROEHLICH[4], Niko KIVEL[5], Dominik KOLL[4], Gunther KORSCHINEK[3], Sarah McINTYRE[4], Silke MERCHEL[6], Stefan PAVETICH[4,6], Georg RUGEL[6], Dorothea SCHUMANN[5], Thomas SMITH[1], and Anton WALLNER[4]

[1]Physics Institute, University of Bern, Sidlerstrasse 5, CH-3012 Bern, Switzerland
[2]IRFU, CEA, Université Paris-Saclay, F-91191, 91190 Gif-sur-Yvette, France
[3]Technical University of Munich (TUM), 80333 Munich, Germany
[4]Department of Nuclear Physics, The Australian National University, Canberra, ACT 2601, Australia
[5]Laboratory of Radiochemistry, Paul Scherrer Institute, CH-5232 Villigen, Switzerland
[6]Helmholtz-Zentrum Dresden-Rossendorf, Bautzner Landstrasse 400, 01328 Dresden, Germany
[*]Corresponding author. E-mail: ingo.leya@space.unibe.ch

(Received 05 August 2019; revision accepted 12 February 2020)

Abstract–We measured specific activities of the long-lived cosmogenic radionuclides ^{60}Fe in 28 iron meteorites and ^{53}Mn in 41 iron meteorites. Accelerator mass spectrometry was applied at the 14 MV Heavy Ion Accelerator Facility at ANU Canberra for all samples except for two which were measured at the Maier-Leibnitz Laboratory, Munich. For the large iron meteorite Twannberg (IIG), we measured six samples for ^{53}Mn. This work doubles the number of existing individual ^{60}Fe data and quadruples the number of iron meteorites studied for ^{60}Fe. We also significantly extended the entire ^{53}Mn database for iron meteorites. The ^{53}Mn data for the iron meteorite Twannberg vary by more than a factor of 30, indicating a significant shielding dependency. In addition, we performed new model calculations for the production of ^{60}Fe and ^{53}Mn in iron meteorites. While the new model is based on the same particle spectra as the earlier model, we no longer use experimental cross sections but instead use cross sections that were calculated using the latest version of the nuclear model code INCL. The new model predictions differ substantially from results obtained with the previous model. Predictions for the ^{60}Fe activity concentrations are about a factor of two higher; for ^{53}Mn, they are ~30% lower, compared to the earlier model, which gives now a better agreement with the experimental data.

INTRODUCTION

Most meteorites are routinely measured by accelerator mass spectrometry (AMS) for the radionuclides ^{10}Be, ^{26}Al, ^{36}Cl, and (more rarely) ^{41}Ca, which, if combined with concentrations for cosmogenic noble gases, provide information on cosmic ray exposure (CRE) histories, that is, CRE ages, terrestrial ages, pre-atmospheric sizes, and shielding depths. In contrast, the data for two other cosmogenic radionuclides, ^{53}Mn ($T_{1/2}$ = 3.7 ± 0.4 Ma; Honda and Imamura 1971) and ^{60}Fe ($T_{1/2}$ = 2.61 ± 0.04 Ma), are scarce because for their measurements dedicated AMS systems are needed to generate ions of 150–200 MeV energy, which is required to reduce the otherwise strongly interfering isobaric background and to achieve a sufficiently high sensitivity. Only two AMS facilities report routine ^{53}Mn and ^{60}Fe measurements. Before AMS, ^{53}Mn has been measured via radiochemical neutron activation techniques (e.g., Imamura et al. 1980), but there are currently only very few suitable nuclear reactors available for such studies.

The ^{60}Fe half-life has been under debate for the last few decades. The value of $T_{1/2}$ = 2.61 ± 0.04 Ma determined by Rugel et al. (2009) was confirmed recently by additional independent measurements (Wallner et al. 2015; Ostdiek et al. 2017). The new value is one order of magnitude higher than the first estimate of $T_{1/2}$ = 0.3 ± 0.9 Ma (Roy and Kohman 1957) and ~75% higher than the previously adopted value of $T_{1/2}$ = 1.49 ± 0.27 Ma (Kutschera et al. 1984).

Another challenge in ^{60}Fe measurements is due to the fact that ^{60}Fe in iron meteorites is only produced from ^{62}Ni and ^{64}Ni. Since both Ni isotopes have a low abundance (^{62}Ni = 3.63%, ^{64}Ni = 0.93%), the ^{60}Fe production rates are relatively low, that is, in the range of disintegration per minute per kg (dpm kg^{-1}) or less (e.g., Knie et al. 1999b; Nishiizumi and Honda 2007). Because the concentration of stable ^{56}Fe atoms is high in meteoritic material, the resulting ^{60}Fe/^{56}Fe ratio is low, that is, in the range 10^{-14}. Such low isotope ratios cannot at present be measured with AMS systems commonly used for ^{10}Be, ^{26}Al, ^{36}Cl, or ^{41}Ca. For ^{53}Mn, it is necessary to remove or suppress the ubiquitous, interfering isobar ^{53}Cr. It is not widely appreciated that this can make an AMS measurement of ^{53}Mn as challenging or even more so than AMS measurements for ^{60}Fe. As a consequence, ^{53}Mn measurements of meteorites require similarly large AMS facilities (~14 MV tandem accelerators) as needed for ^{60}Fe.

Against those odds, ^{53}Mn and ^{60}Fe both have the potential to constrain CRE histories of iron meteorites, potentially even better than the classical lighter radionuclides. First, ^{60}Fe is only produced from a single target element, that is, Ni, and ^{53}Mn is only produced from Fe and Ni. Consequently, neither nuclide is affected by problems caused by variable contributions from the lighter elements sulfur and phosphorous (with the exception of sample dilution, which typically is irrelevant compared to overall uncertainties of the data). Very often microinclusions of troilite (FeS) and schreibersite ([Fe,Ni]P_3) compromise detailed studies of the mainstream cosmogenic nuclides ^{10}Be, ^{26}Al, and ^{21}Ne and therefore limit their use for accurate determination of CRE histories of iron meteorites. Second, due to its relatively long half-life compared to ^{10}Be, ^{26}Al, ^{36}Cl, and ^{41}Ca, ^{53}Mn is less affected by decay during terrestrial residence, which makes the interpretation easier, because most meteorites are finds and not falls. Consequently, although the measurements of ^{53}Mn and ^{60}Fe are more challenging than the measurements of the classical radionuclides, they can provide valuable additional constraints on CRE histories of iron meteorites.

Recently, ^{60}Fe (and in some cases ^{53}Mn) have been analyzed in deep sea materials (crusts, nodules, sediments), Antarctic snow, and the lunar regolith as a tracer for nearby supernova explosions (e.g., Knie et al. 1999a, 2004; Fitoussi et al. 2008; Wallner et al. 2016; Fimiani et al. 2016; Ludwig et al. 2016; Koll et al. 2019a, 2019b; Wallner, personal communication). Considering meteorites, there are only very few studies that include ^{60}Fe. The first ^{60}Fe measurement in a meteorite was performed by Goel and Honda (1965) by decay counting of the radioactive daughter ^{60}Co in 2.5 kg of the chemically processed iron meteorite Odessa. Kutschera (1984) described the first successful ^{60}Fe detection by AMS of a meteorite sample (Treysa). Knie et al. (1999b) presented ^{60}Fe activities in the iron meteorites Dermbach and Tlacotepec and in the metal fractions of the mesosiderite Emery and the LL chondrite Saint-Séverin. More recently, Berger et al. (2007) studied the ^{60}Fe shielding dependence in the three iron meteorites Canyon Diablo, Grant, and Dorofeevka, which cover a large range of different shielding conditions. They found that ^{60}Fe production rates in large iron meteorites decrease with increasing shielding but that the trend in smaller iron meteorites is not that clear; the production rates might also slightly decrease with increasing shielding. In addition, Nishiizumi and Honda (2007) measured ^{60}Fe activities in six iron meteorites using low-level counting and found a good correlation between ^{60}Fe/kg(Ni) and measured ^{53}Mn activities. The Odessa sample studied by Nishiizumi and Honda (2007) was measured before by Goel and Honda (1965). The large discrepancy of a factor of six in specific ^{60}Fe activities was explained by a change of the ^{60}Co half-life in-between the two studies (Nishiizumi and Honda 2007). The latest study that includes both ^{53}Mn and ^{60}Fe was for the very large iron meteorite find Gebel Kamil (Ott et al. 2014). The Gebel Kamil data were used together with data from the aforementioned AMS studies to constrain the activity ratio of ^{60}Fe to ^{53}Mn of $(2.68 \pm 0.35)\times10^{-3}$ (dpm kg^{-1}[Ni]/dpm kg^{-1}[Fe]). This ratio allowed workers to disentangle the cosmogenically produced ^{60}Fe from interstellar ^{60}Fe in lunar and terrestrial material (Fimiani et al. 2016; Koll et al. 2019a, 2019b). To summarize, for the last 12 years, only one meteorite study was published that analyzed both heavy radionuclides.

The data presented here are part of a larger project determining CRE histories of iron meteorites and thereby studying the constancy of galactic cosmic rays (Smith et al. 2019). In the course of this project, we measured cosmogenic noble gas and radionuclide concentrations in ~60 iron meteorites, mainly from group IIIAB. We chemically separated ^{53}Mn and ^{60}Fe and prepared AMS targets for all of them; so far 28 were measured for ^{60}Fe and 41 were measured for ^{53}Mn (plus six additional samples from the large Twannberg iron meteorite). Although the database is not yet complete, it may nevertheless help to better understand the production systematics of ^{53}Mn and ^{60}Fe in iron meteorites and to validate the improved model calculations for cosmogenic nuclide production in meteorites (Ammon et al. 2009).

EXPERIMENTAL

Samples

Most samples are from one of the following museums and research institutes: The Ege University Observatory Research and Application center, Turkey; The Vienna Natural History Museum, Austria; The Field Museum, Chicago, USA; The Department of Mineralogy and Petrology, Poznań, Poland; The Royal Ontario Museum, Toronto, Canada; The "Centre Européen de Recherche et d'Enseignement en Géosciences de l'Environnement" (CEREGE), Aix-en-Provence, France; The London Natural History Museum, London, England; The Senckenberg Natural History Museum, Frankfurt am Main, Germany; The collection at the University of Berne, Switzerland; The collection at ETH Zürich, Switzerland; The American Museum of Natural History, New York, USA. Aliquots of the samples from Braunau, Cincinnati, Forsyth County, North Chile, and Sikhote-Alin were studied earlier by D. Cook for ^{180}W anomalies (Cook et al. 2018). In addition, we studied six samples from the large Twannberg iron meteorite (for the corresponding lighter radionuclides, see Smith et al. 2017).

Sample Preparation

In a related project, all samples have been studied for ^{10}Be, ^{26}Al, ^{36}Cl, and ^{41}Ca as well as for the light cosmogenic noble gases He, Ne, and Ar (Smith et al. 2019). The chemical preparation was performed at the Dresden Accelerator Mass Spectrometry (DREAMS) facility of the Helmholtz-Zentrum Dresden-Rossendorf (HZDR) and was adapted from the procedure described earlier by Merchel and Herpers (1999). A full description of the chemical separation procedure is given by Smith et al. (2017, 2019). Here, we give some details, especially for the ^{53}Mn and ^{60}Fe analysis. The solution from the anion exchange (7.1 M HCl fraction, height 20 cm, diameter 1 cm, DOWEX 1X8, 100–200 mesh) containing mainly Mn was further purified from the interfering isobar ^{53}Cr using the following procedure: First, the solution was evaporated to dryness on a hot plate. The residue was dissolved in a mixture of 5 ml H_2O, 5 ml HNO_3, and 0.5 ml H_2O_2 to reduce Mn^{4+} to Mn^{2+}. The solution was then heated for ~1 h to fully destroy H_2O_2. Subsequently, $KClO_3$ was added to oxidize Mn^{2+} back to Mn^{4+} and finally precipitate it as $MnO(OH)_2$ by heating for ~1 h. This precipitate was rinsed three times with water, subsequently transferred into microreaction vessels (Eppendorf tubes), and finally dried at 80°C in an oven. In an attempt to speed up the chemical processing, we slightly changed the protocol for one sample batch, which resulted in chemical yields larger than 100% (e.g., Turtle River, Elyria, Casas Grandes). An SEM-EDX (scanning electron microscope/energy-dispersive spectroscopy) measurement of these samples revealed that they were contaminated with AgCl from the earlier Ag^{36}Cl AMS target preparation. Hence, we "rescued" the MnO_2 samples by washing them three times with ~12.5% NH_{3aq} solution to dissolve the AgCl. A second SEM-EDX scan of these samples after the cleaning showed that the precipitate was pure MnO_2. We applied the original longer protocol for all remaining samples. The MnO_2 powder was mixed with Ag powder, with a mass ratio MnO_2:Ag = 1:4 and was then pressed into Cu sample holders.

For the ^{60}Fe analysis, the isobar ^{60}Ni introduces an interfering background in AMS, a background that needs to be suppressed during sample preparation. We applied the following procedure: During the anion exchange step, Fe^{3+} is present as a chloro-complex $[FeCl_4]^-$ and is absorbed on the DOWEX 1x8. Nickel is eluted with 10.2 M HCl, while Fe can be stripped after all other elements by elution with H_2O (27 ml). The iron was then precipitated as FeO(OH) by adding ~9 ml of 25% NH_{3aq}. The precipitate was rinsed three times with dilute ammonia solution (i.e., two drops of 25% NH_{3aq} in 250 ml H_2O), then dried as iron oxide in an oven at 90°C, and was later ignited at 800°C for ~2 h. The iron oxide powder was mixed with Ag powder, with a mass ratio Fe_2O_3:Ag ~1:2, and was pressed into Cu sample holders for subsequent AMS measurements.

AMS Measurements

The nuclide ^{60}Fe was measured at the ANU Canberra relative to the PSI-12 standard material, which was produced at the Paul Scherrer Institute (PSI) from a dilution series that is based on material extracted from a beam dump. The ^{60}Fe/Fe ratio of PSI-12 is $1.234(7) \times 10^{-12}$ (Schumann et al. 2019). The original material was used for the half-life measurements of ^{60}Fe (e.g., Rugel et al. 2009). The Munich group used a primary standard with a concentration of ^{60}Fe/Fe = $(9 \pm 1) \times 10^{-12}$, which is described in Knie et al. (1999a, 1999b). All ^{53}Mn measurements were performed at the ANU Canberra relative to a piece of the Grant iron meteorite that was provided by Greg Herzog (personal communication); the nominal ^{53}Mn/^{55}Mn ratio is 2.59×10^{-10} (Gladkis 2006). This value has been obtained measuring the ^{53}Mn activity in 200 g of the iron meteorite Grant via the ^{53}Cr K_α-line. The ratio used at ANU is 10% lower than the value used by others.

Note that a change in AMS standards and/or half-lives has a direct influence on the meteorite data. If we consider, as an example, the radionuclide ^{60}Fe we measure the concentration of ^{60}Fe atoms in a sample, whereas the given production rates are saturation activities calculated via decay constant times the nuclide concentration. The recent change in the half-life of 75%, therefore, reduces the production rates by the same 75%. Consequently, all data that are based on the old half-life must be reduced by 75% to be comparable to the new measurements.

ANU Canberra: Samples were loaded into an MC SNICS ion source that is equipped with a sample wheel holding up to 32 positions. Either MnO^- (for ^{53}Mn) or FeO^- (for ^{60}Fe) was extracted and injected into the 14UD tandem accelerator at the Heavy Ion Accelerator Facility (HIAF; Fifield et al. 2013; Wallner et al. 2015). For these measurements, the 14UD accelerator was operated at terminal voltages between 13.8 and 14.3 MV. By selecting charge states of 11+ for Fe and 12+ or 13 + for Mn, we obtained particle energies between 165 MeV for ^{60}Fe and up to 200 MeV for ^{53}Mn. Typical currents were several μA of FeO^- and several 100 nA for MnO^-. Beam intensities of the stable isotopes ^{54}Fe, ^{56}Fe, and ^{55}Mn, respectively, were measured with Faraday cups at the low- and high-energy side of the spectrometer. The rare isotopes ^{53}Mn and ^{60}Fe were directed into a gas-filled magnet (ENGE spectrometer converted into gas-filled mode) and then counted atom by atom in a multi-anode ionization chamber (Fifield et al. 2013; Martschini et al. 2019). The gas-filled magnet allows for a spatial separation of the stable isobar from the radionuclide due to their different mean charge states and therefore different deflection angles caused by the interaction with the gas. This separation blocks the majority of the stable isobars from entering the particle detector and consequently reduces the beam intensity of the background isobars in the ionization chamber to acceptable levels (typically less than 100 ^{60}Ni and up to a few 1000 ^{53}Cr events per second). The background for ^{60}Fe was measured as low as $^{60}Fe/Fe = 3\times10^{-17}$ (typical blanks for our study $^{60}Fe/Fe \sim 10^{-16}$; Wallner, personal communication) and the ^{53}Mn- background was in the range $^{53}Mn/^{55}Mn < 10^{-12}$. The reproducibility of the AMS measurements, based on repeated measurements of identical samples, is ~3–5% for ^{60}Fe and ~5–10% for ^{53}Mn, respectively.

TUM Munich: The AMS facility in Munich at the Maier-Leibnitz-Laboratory in Garching is also based on a 14 MV tandem accelerator combined with a gas-filled analyzing magnet system. The isobaric background for the ^{60}Fe measurements was reduced in the same way as described above for the ANU Canberra setup (Knie et al. 2000; Koll et al., 2019a, 2019b).

NEW MODEL CALCULATIONS

Our previous calculations modeling the production rates of ^{53}Mn and ^{60}Fe were based on the nuclear reaction cross sections that were available at that time (Merchel et al. [2000] and references therein), on adjusted cross sections for the neutron-induced reactions (Ammon et al. 2009; Leya and Michel 2011), and on the depth- and size-dependent spectra for primary and secondary particles calculated using Monte Carlo methods. For the production of ^{53}Mn from ^{nat}Ni and ^{60}Fe from ^{nat}Ni, the cross section database was limited and/or the data scattered far outside the range of the given uncertainties (e.g., Merchel et al. [2000] and references therein; Ammon et al. 2009). The earlier model predictions for ^{53}Mn overestimated measured-specific activities for the meteorite Grant by up to 50%, which Ammon et al. (2009) argued could be due to AMS normalization problems for the proton-induced cross sections and/or the thick target production rates used to determine the neutron-induced cross sections. Note that such problems would only partially cancel out during the adjustment procedure used to determine the neutron-induced cross sections.

As already stated by Ammon et al. (2009), the model predictions for the production of ^{60}Fe were much lower than most of the experimental data. The calculated upper limit for the ^{60}Fe-specific activity was ~0.9 dpm kg^{-1}(Ni) and was at the center of a 25 cm iron meteoroid. Since then, the recommended half-life value for ^{60}Fe has seen an increase of ~75%. Consequently, it is possible that the discrepancies between the earlier model predictions and the experimental data were (at least partly) caused by problems related to the experimental input data used for modeling, that is, proton-induced cross sections and/or thick target production rates used to determine neutron-induced cross sections. Here, we try to overcome the problem by using only calculated cross sections for modeling. In doing so, we rely on the latest version of the INCL (Liège Intra Nuclear Cascade) code, which has recently been improved for higher energies, that is, in the range above 1 GeV, and for the emission of light complex particles (e.g., David et al. 2013; Mancusi et al. 2015; Pedoux and Cugnon 2011). We consider the current version of the code to be for the first time reliable enough for calculating sufficiently accurate production rates. The depth- and size-dependent energy spectra of primary and secondary particles used for modeling have been calculated using Monte Carlo methods, and they are the same as used by Ammon et al. (2009), that is, we use a solar modulation parameter M = 550 and a particle flux in the meteoroid orbits of 4.47 cm^{-2} s^{-1}.

Manganese-53: The proton- (solid line) and neutron- (dashed line) induced cross sections calculated by INCL for the production of ^{53}Mn from ^{nat}Fe are shown in Fig. 1 (upper panel). Also shown are the experimental cross sections for the proton-induced production given by Furukawa (1973), Gensho et al. (1972, 1979), Kumabe et al. (1963), Lavrukina et al. (1964), Shore et al. (1961), Perron (1976), and Merchel et al. (2000). In addition, we show the data for the reaction ^{56}Fe(p, X)^{53}Mn obtained in inverse kinematics experiments (Villagrasa-Canton et al. 2007). With an ^{56}Fe abundance of 92%, the inverse kinematics data for ^{56}Fe should be comparable to the other data obtained by irradiating Fe with a natural isotopic composition. It can be seen that the experimental data give a consistent excitation function, at least up to ~60 MeV incident proton energy. In the energy range 400–1600 MeV, the data scatter significantly. Conversely, the INCL model produces a smoother excitation function. For energies below ~40 MeV, the experimental cross sections are significantly higher than the model predictions and also the threshold energies differ. Whereas the model predicts a threshold energy of ~14 MeV, the experimental data show the production of ^{53}Mn already at 12 MeV; the difference is important because reactions with lower reaction thresholds very often produce higher meteorite production rates. Above 40 MeV, there is reasonable agreement between measured and calculated cross sections. Also shown are the modeled results for the neutron-induced production of ^{53}Mn from ^{nat}Fe. Below ~40 MeV, the neutron-induced cross sections are higher than the proton-induced data by up to a factor of two (the average is 40%); at the local minimum close to 40 MeV, they are lower than the proton-induced cross sections by up to 50%, and they are again ~20% larger than the proton data for energies between 40 MeV and 65 MeV. For energies in the range 65 MeV–1 GeV, the proton-induced cross sections are on average 20% larger than the neutron-induced cross sections. Above 1 GeV, the cross sections for both projectile types are similar.

The proton- (solid line) and neutron-induced (dashed line) cross sections for the production of ^{53}Mn from ^{nat}Ni are shown in the middle panel of Fig. 1. Also shown are the experimental data from Merchel et al. (2000). While there is a reasonable agreement between experimental and calculated data, the experimental data are too scarce for establishing an excitation function consistent enough for model calculations. Again, the INCL calculations produce a smooth excitation function.

The new model predictions for cosmogenic ^{53}Mn production in iron meteoroids with pre-atmospheric radii of 5, 10, 15, 25, 30, 32, 40, 50, 60, 65, 85, 100,

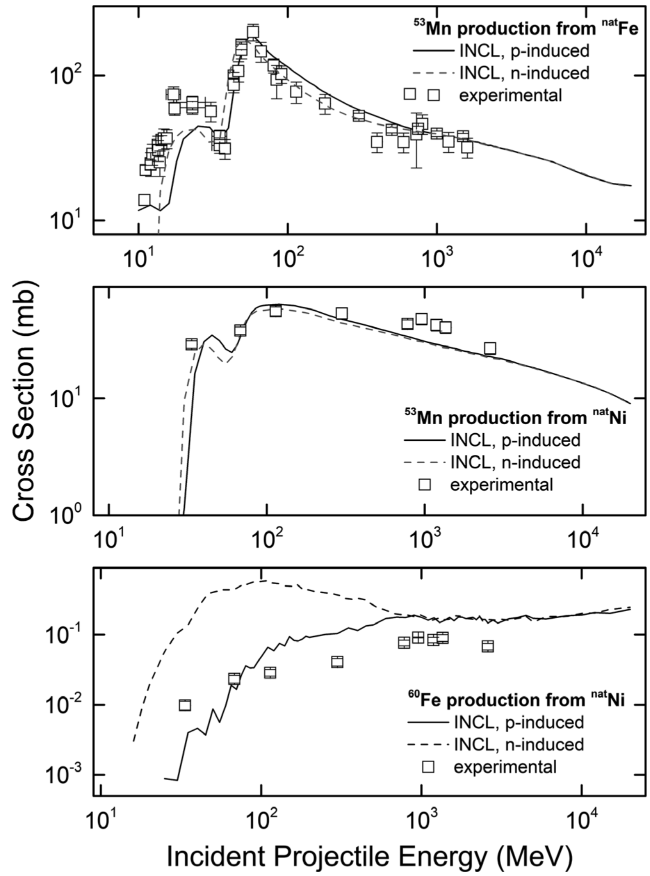

Fig. 1. Cross sections for the proton- and neutron-induced production of ^{53}Mn from ^{nat}Fe (upper panel), ^{nat}Ni (middle panel), and of ^{60}Fe from ^{nat}Ni (lower panel). Shown are the results from the INCL calculations (solid and dashed lines) and experimental data. The experimental data for the proton-induced production are from Furukawa (1973), Gensho et al. (1972, 1979), Kumabe et al. (1963), Lavrukina et al. (1964), Shore et al. (1961), Perron (1976), Merchel et al. (2000), and Villagrasa-Canton et al. (2007) and are not corrected for the new half-life value.

120 cm, and for the outermost 200 cm of a 10 m object calculated using the new proton- and neutron-induced cross sections are shown in Fig. 2. The ^{53}Mn production is for almost all radii and all shielding depths dominated by neutrons. For example, already at the center of a 5 cm iron meteoroid more than 50% of ^{53}Mn is produced by secondary neutrons. This value increases to ~80% at the center of a 25 cm iron meteoroid and reaches more than ~90% at the center of a 50 cm iron meteoroid.

The specific ^{53}Mn activities for iron meteorites found in literature are between 23 ± 1 dpm kg^{-1} and 583 ± 25 dpm kg^{-1} (e.g., Nishiizumi et al. 1991), which is in good agreement with the range 33–567 dpm kg^{-1} predicted by the model. Furthermore,

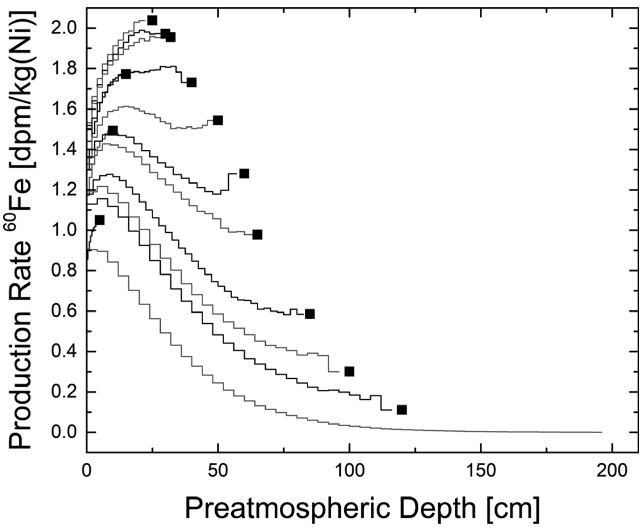

Fig. 2. Depth- and size-dependent production rates of ^{53}Mn in iron meteoroids with pre-atmospheric radii of 5, 10, 15, 25, 30, 32, 40, 50, 60, 65, 85, 100, 120 cm and in the outermost 200 cm of a 10 m object.

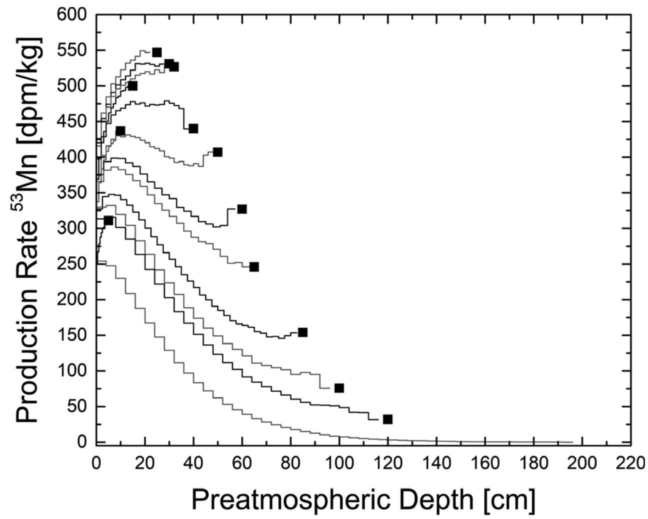

Fig. 3. Depth- and size-dependent production rates of ^{60}Fe in iron meteoroids with pre-atmospheric radii of 5, 10, 15, 25, 30, 32, 40, 50, 60, 65, 85, 100, 120 cm and in the outermost 200 cm of a 10 m object.

Honda et al. (1961) measured ^{53}Mn in the four iron meteorites Grant, Williamstown, Odessa, and Canyon Diablo and found production rates in the range 92 ± 12–299 ± 11 dpm kg^{-1}, again in the range of the model predictions. However, there is a slight discrepancy for the iron meteorite Grant. While the model predicts ^{53}Mn production rates in the range 342–500 dpm kg^{-1} for an iron meteoroid with a radius of 40 cm, Honda et al. (1961) measured a production rate of 299 ± 11 dpm kg^{-1}. In a later measurement of the iron meteorite Grant, Imamura et al. (1980) measured specific ^{53}Mn activities between 304 ± 15 and 374 ± 16 dpm kg^{-1}, still somewhat low but slightly closer to the model predictions. The ^{53}Mn AMS value by Merchel (1998) of 435 ± 65 dpm kg^{-1} fits perfectly with the new model.

Iron-60: Our new purely theoretical data support the statement that the earlier experiment-based model significantly underestimated the ^{60}Fe production rates in iron meteorites as 21 of 28 of the obtained data are higher than the (former) modeled upper limit. Figure 1 (lower panel) depicts the INCL results for the proton- (black solid line) and neutron-induced (dashed line) production of ^{60}Fe from ^{nat}Ni. Also shown are the experimental data from Merchel et al. (2000) for the proton-induced production. Note that changing the half-life from 1.49 to 2.61 Ma will not change the cross sections, because the change in the measured activity cancels with the factor accounting for saturation. The two major reactions for the proton-induced production of ^{60}Fe are ^{62}Ni(p,3p)^{60}Fe and ^{64}Ni(p,3p2n)^{60}Fe or ^{64}Ni (p,αp)^{60}Fe (i.e., an alpha particle instead of two protons and two neutrons in the exit channel). Most importantly and very surprisingly, the cross sections for the neutron-induced production of ^{60}Fe from Ni are up to five times higher than the cross sections for the proton-induced production. The most relevant reactions for the neutron-induced production of ^{60}Fe are ^{62}Ni(n,2pn)^{60}Fe and ^{64}Ni(n,2p3n)^{60}Fe or ^{64}Ni(n, αn)^{60}Fe. The results of the new model calculations are shown in Fig. 3 as depth-dependent production rates for iron meteorites with pre-atmospheric radii of 5, 10, 15, 25, 30, 32, 40, 50, 60, 65, 85, 100, 120 cm, and for the outermost 200 cm of a 10 m object.

RESULTS AND DISCUSSION

The ^{60}Fe/^{56}Fe and ^{53}Mn/^{55}Mn ratios of the meteorite samples measured by AMS have been normalized to the standards for ^{53}Mn and ^{60}Fe. Based on analyses by inductively coupled plasma mass spectrometry (ICP-MS) on stable Fe (calculated from the ICP-MS data for Ni via Fe [%] = 100% – Ni [%]), ^{60}Fe atoms have been calculated from the measured ^{60}Fe/Fe ratios. Finally, ^{60}Fe-specific activities (dpm kg^{-1}[Ni]) have been calculated by using the ICP-MS data for Ni and the half-life of ^{60}Fe. For ^{53}Mn, the normalized AMS ratios were converted to ^{53}Mn atoms by using the value for ^{55}Mn atoms from the added carrier. As ^{53}Mn is given in units of dpm kg^{-1}, no ICP-MS data was involved in calculating ^{53}Mn activity values, but the half-life was used to convert the number of measured atoms into activities.

^{53}Mn Activities in Iron Meteorites

The ^{53}Mn data for the 46 samples from 41 meteorites are given in Table 1. For the large iron meteorite Twannberg, we studied six samples. The terrestrial ages used below are from the study by Smith et al. (2019). Owing to the long half-life of ^{53}Mn, decay corrections due to the terrestrial residence are insignificant, that is, the measured activity concentrations can just be converted to production rates. Note that even the longest terrestrial age of 285 ka for Puentel del Zacate reduces the ^{53}Mn concentration by less than 5%, which is below typical uncertainties for the AMS measurements (note that no ^{53}Mn has been measured for Puentel del Zacate). The ^{53}Mn activities based on the AMS measurements range from 4.3 to 658 dpm kg^{-1}. Considering only Twannberg samples, the ^{53}Mn activities range from 4.3 to 165 dpm kg^{-1}, that is, the spread is almost a factor of 40. Such a large spread for data from one meteorite confirms the large pre-atmospheric size of Twannberg (see also below). For the iron meteorite Grant, we measured a ^{53}Mn production rate of 441 ± 45 dpm kg^{-1}, which is significantly higher than the ^{53}Mn production rates given by Imamura et al. (1980), which range between 304 ± 15 and 374 ± 16 dpm kg^{-1}.

The new model predictions for ^{53}Mn are between ~20% (surface of small meteoroids) and ~30% (center of large meteoroids) lower than the previous model predictions (Ammon et al. 2009). Averaged over all radii and all shielding depths, the difference is ~30%. With the new ^{53}Mn data for Grant and the new model calculations, there is now a good agreement between experimental data and model predictions. For example, the model predicts ^{53}Mn-specific activities in the range 331–478 dpm kg^{-1}, in very good agreement with the measured specific activity of 441 ± 45 dpm kg^{-1}.

Nevertheless, there are still some discrepancies between model predictions and experimental data. For example, the model predicts maximum ^{53}Mn production rates of 547 dpm kg^{-1} in the center of a 25 cm meteoroid (Fig. 2). In contrast, the ^{53}Mn production rate for 8 of the 41 studied meteorites (Avoca, Bristol, Calico Rock, Chulafinne, Dalton, Fort Pierre, Greenbrier County, Zerhamra) is higher than the upper limit given by the model. For seven of the eight meteorites, however, there is agreement within the 1σ standard deviation; the only exception is Chulafinne, for which the agreement is only within the 2σ standard deviation.

We now discuss the shielding dependence of the ^{53}Mn data for Twannberg. The model predicts that for an iron meteoroid of radius 120 cm, the production rate varies only by a factor of ~10 with shielding, compared to the measured factor of 40. Consequently, Twannberg must have been larger than 120 cm in radius. Moreover, ^{53}Mn activities as low as 4.26 dpm kg^{-1} as measured for one of the Twannberg samples are only possible at a depth of 120 cm in an object with a radius of 10 m (e.g., Smith et al. 2017). Larger depths in smaller objects (1.2 m <radius <10 m) are also possible; however, we have no model predictions for such objects.

^{60}Fe Activities in Iron Meteorites

The ^{60}Fe concentrations normalized to the Ni content of the 28 iron meteorites are compiled in Table 1. The calculated specific activities range from 0.38 dpm kg^{-1}(Ni) for Casas Grandes to 2.02 dpm kg^{-1}(Ni) for Gan Gan. The new ^{60}Fe data are in the range of values found in the literature for other iron meteorites (recalculated for the new half-life). For example, Casas Grandes and Lombard have low ^{60}Fe activities of 0.38 dpm kg^{-1}(Ni) and 0.46 dpm kg^{-1}(Ni), respectively. Such low concentrations have also been determined in the large meteorites Gebel Kamil (Ott et al. 2014) and Canyon Diablo (Berger et al. 2007).

For further discussion, we calculate production rates, that is, we correct the ^{60}Fe activities for radioactive decay during terrestrial residence. The terrestrial ages have been determined using ^{41}Ca/^{36}Cl atom ratios (Smith et al. 2019). The changes are minor; the maximum is 7% for Casas Grandes (terrestrial age of 247 ± 98 ka) and the average change is 1%. The calculated production rates are given in Table 1 as ^{60}Fe (0; dpm kg^{-1}[Ni]). Figure 4 depicts a histogram of all existing (to our knowledge) ^{60}Fe data for iron meteorites. In addition to our new data (Table 1), literature data from Knie et al. (1999b), Nishiizumi and Honda (2007), Berger et al. (2007), and Ott et al. (2014) are included. The data from Knie et al. (1999b), Berger et al. (2007), and Nishiizumi and Honda (2007) have been recalculated for the new ^{60}Fe half-life.

The new model calculations for ^{60}Fe production rates are significantly higher than the earlier model by Ammon et al. (2009). While the maximum is still at the center of a 25 cm meteoroid, it is now slightly above 2 dpm kg^{-1}(Ni), that is, more than a factor of 2 higher (see Fig. 3). Since for most of the studied meteorites neither the pre-atmospheric radius nor the pre-atmospheric shielding depth of the studied sample is known, a comparison of the experimental data with the model predictions is only possible for production rate averages and ranges. The improved model is in accord with measured activities. For example, the predicted ^{60}Fe production rates for all shielding depths in iron meteoroids with radii between 5 and 120 cm range

Table 1. Name of studied meteorites, chemical group, found mass, ^{53}Mn (dpm kg^{-1}) and ^{60}Fe (dpm kg^{-1}[Ni]) activity concentrations, Ni concentrations, and ^{60}Fe production rates ^{60}Fe(0; dpm kg^{-1}[Ni]).

Samples	Group	Found mass [kg]	^{53}Mn (dpm kg^{-1})	^{60}Fe (dpm kg^{-1} Ni)	Ni (%)	^{60}Fe(0) (dpm kg^{-1} (Ni))
Arispe	IIIAB	683	325 ± 51	–	6.20	–
Avoca	IC	37.85	580 ± 107	1.14 ± 0.20	9.15	1.16 ± 0.20
Benedict	IIIAB	16.38	*19.3 ± 1.6*[a]	1.37 ± 0.23	8.85	1.37 ± 0.23
Braunau	IIAB	39	310 ± 38	–	5.11	–
Bristol	IVA	20	658 ± 159	–	8.49	–
Brownfield	IIAB	1.63	476 ± 49	–	10.31	–
Calico Rock	IIAB	7.28	555 ± 52	–	5.58	–
Cape York	IIIAB	58.2 tons	18.6 ± 1.9	–	8.38	–
Carthage	IIIAB	127	390 ± 64	–	11.11	–
Casas Grandes	IIIAB	1.55 tons	237 ± 29	0.35 ± 0.13	7.77	0.38 ± 0.14
Charcas	IIIAB	1.4 tons	334 ± 52	1.21 ± 0.25	8.60	1.25 ± 0.26
Chulafinne	IIIAB	16.22	607 + 38	2.15 ± 0.31	10.50	2.16 ± 0.31
Cincinnati	IIAB	1.5	469 ± 47	–	8.70	–
Dalton	IIIAB	53	571 ± 45	–	12.57	–
Durango	IIIAB	164	441 ± 44	0.99 ± 0.19	10.90	1.03 ± 0.20
Elyria	IIIAB	10.9	439 ± 44	1.21 ± 0.22	8.68	1.22 ± 0.23
Forsyth County	IIAB	22.7	534 ± 54	–	5.03	–
Fort Pierre	IIIAB	15.9	610 ± 99	1.60 ± 0.28	7.52	1.60 ± 0.28
Gan Gan[b]	IVA	83	323 ± 14	2.02 ± 0.37	9.51	2.02 ± 0.37
Gibeon	IVA	26 tons	2.87 ± 0.41	–	8.37	–
Grant	IIIAB	525	441 ± 45	–	7.17	–
Greenbrier County	IIIAB	5	630 ± 86	1.43 ± 0.19	6.85	1.45 ± 0.20
Joel's Iron	IIIAB	1.3	420 ± 94	1.42 ± 0.21	8.74	1.43 ± 0.21
Kayakent	IIIAB	85	–	1.32 ± 0.23	7.28	1.32 ± 0.23
Lombard	IIAB	7	159 ± 33	0.46 ± 0.13	5.42	0.46 ± 0.13
Mapleton	IIIAB	49	–	1.85 ± 0.25	7.52	1.85 ± 0.25
Norfolk	IIIAB	23	344 ± 67	0.82 ± 0.16	7.14	0.82 ± 0.16
North Chile	IIAB	300	97.7 ± 9.4	–	5.23	–
Picacho	IIIAB	22	–	1.35 ± 0.22	7.44	1.39 ± 0.22
Piñon[b]	Ungr.	17.85	303 ± 13	0.95 ± 0.16	16.57	0.95 ± 0.17
Plymouth	IIIAB	14	501 ± 27	1.00 ± 0.21	11.52	1.01 ± 0.21
Puentel del Zacate	IIIAB	30.79	–	0.36 ± 0.06	8.54	0.39 ± 0.06
Roebourne	IIIAB	86.86	539 ± 54	–	9.04	–
Rowton	IIIAB	3.5	340 ± 36	1.18 ± 0.17	7.04	1.18 ± 0.17
Sacramento Mountains	IIIAB	237.2	491 ± 82	1.59 ± 0.25	7.74	1.65 ± 0.26
San Angelo	IIIAB	88	332 ± 37	0.73 ± 0.13	9.19	0.75 ± 0.13
Schwetz	IIIAB	21.5	500 ± 49	1.07 ± 0.20	7.17	1.07 ± 0.20
Sikhote-Alin	IIAB	23 tons	358 ± 35	–	5.62	–
Squaw Creek	IIAB	14.5	–	1.65 ± 0.31	5.69	1.68 ± 0.31
Tamentit	IIIAB	510	493 ± 54	1.25 ± 0.22	10.17	1.26 ± 0.22
Trenton	IIIAB	505	516 ± 52	–	7.91	–
Treysa	IIIAB	63	384 ± n/na[c]	1.14 ± 0.15	8.63	1.14 ± 0.15
Turtle River	IIIAB	22.39	56.4 ± 6.4	0.88 ± 0.17	9.16	0.89 ± 0.17
Verkhne Udinsk	IIIAB	18	491 ± 76	–	7.35	–
Zerhamra	IIG	630	598 ± 91	1.10 ± 0.22	8.77	1.10 ± 0.22
Twannberg—TW 3	IIG		139 ± 20	–	4.04	–
TW 7	IIG		4.3 ± 0.5	–	4.37	–
TW 15	IIG		50. ± 4.	–	4.81	–
TW 39	IIG		45 ± 10	–	4.30	–
TW 84	IIG		165 ± 40	–	4.67	–
TW 87	IIG		19 ± 6	–	4.63	–

[a]Sample might have been lost during chemical processing (see text).
[b]Samples where ^{53}Mn was measured at the Maier-Leibnitz-Laboratory AMS facility in Munich. All other samples were measured at the ANU Canberra.
[c]Cannot be given.

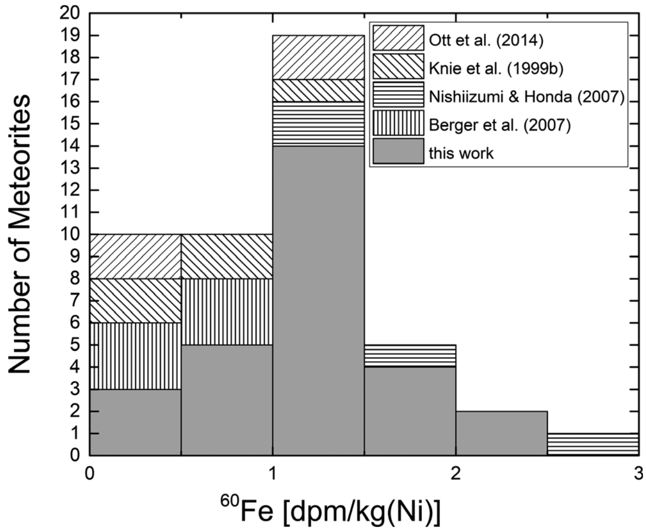

Fig. 4. Histogram of ^{60}Fe activities (dpm kg^{-1}[Ni]) of the 28 studied meteorites. Also shown are data from the literature (Ott et al. 2014; Berger et al. 2007; Nishiizumi and Honda 2007; Knie et al. 1999b). The data from Knie et al. (1999b), Berger et al. (2007), and Nishiizumi and Honda (2007) were recalculated for the now accepted ^{60}Fe half-life of $T_{1/2}$ = 2.61 ± 0.04 Ma (Rugel et al. 2009).

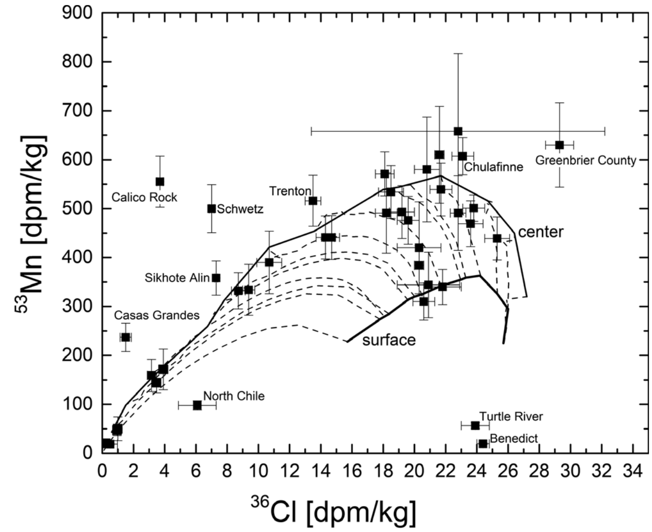

Fig. 5. Production rates of ^{53}Mn as a function of ^{36}Cl production rates for all shielding depths in iron meteorites with pre-atmospheric radii between 5 cm and 120 cm and the outermost 2 m of a 10 m object. The thin dotted lines connect the model calculations for an individual meteorite (from the surface toward the center). The thick black lines connect the results for all surfaces and centers, respectively. The model predictions define an area of allowed ^{36}Cl-^{53}Mn production rate combinations. Also shown are experimental data. Meteorites plotting outside the allowed field are labeled.

between 0.2 and 2 dpm kg^{-1}(Ni), which covers all of the measured ^{60}Fe activities.

Again, there are still some discrepancies between model predictions and experimental data. The modeled ^{60}Fe production rates for an iron meteorite with a radius of 40 cm, that is, very close to the pre-atmospheric radius of Grant (Ammon et al. 2008), vary between 1.2 dpm kg^{-1}(Ni) and 1.8 dpm kg^{-1}(Ni). This is significantly higher than the measured data for Grant from Berger et al. (2007), which are—after recalculating them using the new ^{60}Fe half-life—0.57 dpm kg^{-1}(Ni) and 0.69 dpm kg^{-1}(Ni). According to the model, such low ^{60}Fe activities are only reached in objects at least 100 cm in radius, which is unreasonable for Grant (e.g., Ammon et al. 2008).

Nuclide Correlations

To search for cosmogenic nuclide correlations that might help decipher cosmic ray exposure histories in iron meteorites, we plot in Fig. 5 the ^{53}Mn production rates as a function of ^{36}Cl production rates for the studied samples. Also shown are the results from the new model predictions for all shielding depths in meteorites with pre-atmospheric radii between 5 and 120 cm and the outermost 2 m of a 10 m radius object (dashed lines). The two solid black lines connect the results for the centers and the surfaces, respectively. The model calculations define an area of allowed ^{36}Cl-^{53}Mn production rates for meteorites that fall within the above-mentioned size range and that experienced single-stage exposure histories. The solid black symbols are experimental data; the ^{53}Mn data are from Table 1; and the ^{36}Cl production rates, which were determined in the same aliquots, are from Smith et al. (2017, 2019). In total, we have ^{36}Cl and ^{53}Mn data for 35 iron meteorites; of these, 25 plot within and 10 plot outside the allowed data field. The three meteorites North Chile, Turtle River, and Benedict plot below the allowed data field. The ^{36}Cl production rates for all three meteorites are in a range typical for iron meteorites, that is, they range between ~6 dpm kg^{-1} for North Chile and ~24.4 dpm kg^{-1} for Benedict. In contrast, the ^{53}Mn production rates are very low. For example, with a ^{36}Cl production rate of 23.9 ± 0.9 dpm kg^{-1} for Turtle River, the model predicts ^{53}Mn production rates in the range 360–530 dpm kg^{-1}, that is, far higher than the 56.4 dpm kg^{-1} measured by us. According to the model calculations, ^{53}Mn production rates as low as 56.4 dpm kg^{-1} are only possible in iron meteorites with pre-atmospheric radii larger than ~100 cm. This is in contrast to the relatively low ^{4}He/^{21}Ne ratio of ~220 and the activity ratios of the light cosmogenic radionuclides (e.g., Smith et al. 2019). The reason for the apparently *too low* ^{53}Mn production rates is not clear. It might be due to (1) a complex exposure history, (2) unrecognized problems during sample preparation and/or AMS measurements, and/or (3) an unusually high concentration of natural ^{55}Mn in the studied iron meteorite. For the last point, we discuss as an example the data for Turtle River. The studied sample had a mass of 102 mg, and during chemical extraction, we added ~4 mg of Mn carrier. For calculating specific ^{53}Mn activities, we used the measured $^{53}Mn/^{55}Mn$ ratio, the amount of ^{55}Mn carrier added, and we assumed that the concentration of native ^{55}Mn in the sample is negligible. Consequently, calculating an ^{53}Mn activity ~10% too low requires in addition to the 4 mg of ^{55}Mn carrier added ~0.4 mg of native ^{55}Mn in the sample. This value is unreasonably high considering that the Mn/Fe ratio in iron meteorites is in the range 10^{-7} (e.g., Sugiura and Hoshino 2003), which corresponds to ~10 ng of native ^{55}Mn in the Turtle River sample, which is lower by more than four orders of magnitude. In addition, Herpers et al. (1969) measured native ^{55}Mn concentrations in the range <5.5–199 ppm, again too low to compromise ^{53}Mn-specific activity measurements by AMS. Next, we consider the second possibility, a complex exposure history. Doing so, we assume a recent break-up of an originally much larger Turtle River iron meteorite. The recovered mass of Turtle River is ~23 kg, which corresponds to a minimum pre-atmospheric radius of ~9 cm (after the hypothetical recent break-up). The ^{36}Cl production rate in such an object is ~25 dpm kg^{-1}, that is, very close to the measured value. To reach this value, the meteorite must have been irradiated for at least 1 Ma. During the same time, 80 dpm kg^{-1} ^{53}Mn would have been produced in such a meteorite, that is, much more than measured by us for Turtle River. Therefore, a complex exposure with a very recent break-up leaving some of the radionuclides under-saturated cannot explain the measured data, leaving unrecognized problems during sample preparation and/or AMS measurements the most likely explanation. Indeed, Turtle River belongs to the batch for which some samples had "virtual" chemical yields larger than 100% for Mn and needed reprocessing (note that the excess was not MnO_2 but AgCl, see above). For Benedict, we cannot completely exclude that the sample (or at least parts of it) got lost during chemical processing. However, there are no indications for any such problems for the North Chile sample.

There are also five meteorites (Casas Grandes, Sikhote-Alin, Calico Rock, Schwetz, Trenton) for which the ^{36}Cl and the ^{53}Mn data individually fall into the allowed range, but for which the combination of ^{36}Cl and ^{53}Mn data are outside the range predicted by the model. For the five meteorites in question, the ^{53}Mn production rates are higher than expected based on the model calculations. Note, however, that our data for Casas Grandes of 237 ± 29 agree well with the 210 ± 6 dpm kg^{-1} measured by Herpers et al. (1969). For Sikhote-Alin, we measured 358 ± 35 dpm kg^{-1} and Herpers et al. (1969) measured 335 ± 8 dpm kg^{-1}, again a good agreement. Finally, Herpers et al. (1969) measured 590 ± 14 dpm kg^{-1} compared to the 516 ± 52 dpm kg^{-1} measured by us. However, to be more precise, the ^{53}Mn data for Calico Rock, Schwetz, and Trenton with greater than 500 dpm kg^{-1} are, according to the model calculations, only possible for iron meteorites with pre-atmospheric radii in the range 20–40 cm. For meteorites in this size range, however, the ^{36}Cl production rates are ~20 dpm kg^{-1} (e.g., Smith et al. 2019), that is, far higher than the values of less than ~14 dpm kg^{-1} measured for two of the three meteorites in question. The found masses of 7.28 kg, 21.5 kg, and 505 kg for Calico Rock, Schwetz, and Trenton are in accord with pre-atmospheric radii in the range 20–40 cm. While we cannot fully exclude that the ^{36}Cl data are too low, we infer that the ^{53}Mn data are too high, which might be caused by unrecognized problems during sample preparation and/or AMS measurements, or it could be due to a complex exposure history. The latter might be as follows: The ^{53}Mn production rate decreases more slowly with depth than the ^{36}Cl production rate. For example, the ^{53}Mn production rate in a 10 m object decreases from the surface toward a shielding depth of ~2 m by about three orders of magnitude. In contrast, the ^{36}Cl production rates decrease by about four orders of magnitude in the same range of shielding depths. Consequently, there are regions in a large iron meteoroid with measurable amounts of ^{53}Mn but without any ^{36}Cl. If, after further break-up, those regions get close to the (new) pre-atmospheric surface, they might have inherited some excess ^{53}Mn from the first irradiation stage leading to high $^{53}Mn/^{36}Cl$ activity ratios. For the break-up to have a measurable effect on the $^{53}Mn/^{36}Cl$ ratio, a requirement would be that it occurred during the last few half-lives of ^{53}Mn, that is, within the last 10 Ma or so. While we consider it as unlikely that such a recent break-up has remained unnoticed so far, considering the variety of measured cosmogenic nuclides (e.g., Smith et al. 2019), such a scenario is not impossible. However, such a scenario cannot explain the data for the five meteorites in question. We discuss here as an example the data for the meteorite Calico Rock. Assuming after the hypothetical recent break-up, a relatively large object with a ^{36}Cl production rate in the range 4 dpm kg^{-1} (close to the value measured by us), the ^{53}Mn production rate would be ~200 dpm kg^{-1}, that is, far lower than the 500 dpm kg^{-1} measured by us. Consequently, in such a scenario, 300 dpm kg^{-1} of ^{53}Mn must have been inherited from the earlier irradiation stage. From Fig. 5, we can conclude that at least in the range of studied pre-atmospheric radii, there is no region in an iron meteorite in which 300 dpm kg^{-1} ^{53}Mn is produced without any collateral production of ^{36}Cl, making such a scenario impossible. A special case is the data for Greenbrier County; the ^{36}Cl data of 29 dpm kg^{-1} are unexpectedly high, whereas according to the model calculations (Smith et al. 2017), the upper limit for the ^{36}Cl production rate in meteoritic metal is $\sim$25 dpm kg^{-1}. Currently, however, we have no reason to consider the ^{36}Cl data for Greenbrier County as unreliable. We might speculate that neutron-capture reactions on natural chlorine might be the reason for the too high ^{36}Cl concentrations. Such a mineral could be lawrencite, which occurs in some iron meteorites (e.g., Goldschmidt 1954; Honda et al. 1961). For a discussion, see also Smith et al. (2019).

The new model predicts $^{60}Fe/^{53}Mn$ production rate ratios in the relatively narrow range 0.0021–0.0031 (dpm kg^{-1}[Ni]/dpm kg^{-1}); the average for all radii and all shielding depths is $(2.8 \pm 0.1) \times 10^{-3}$. Considering now that the model calculations are for metal consisting of 90% Fe and 10% Ni, the production rate ratio ^{60}Fe $(kgNi)^{-1}$ to ^{53}Mn $(kgFe)^{-1}$ changes to $(2.5 \pm 0.1) \times 10^{-3}$. This is in excellent agreement with the activity ratio of ^{60}Fe $(kgNi)^{-1}$ to ^{53}Mn $(kgFe)^{-1}$ of $(2.68 \pm 0.35) \times 10^{-3}$ deduced by Fimiani et al. (2016) for meteorite data, which has been used by these authors to disentangle measured ^{60}Fe data for lunar Apollo 12, 15, and 16 samples into cosmogenic and interstellar components. Both activity ratios are slightly higher than the ratios expected for extraterrestrial dust ($^{60}Fe/^{53}Mn$ $\sim 10^{-4}$ dpm kg^{-1}[Ni]/dpm kg^{-1}; Knie et al. 1999a).

Figure 6 depicts the ^{60}Fe production rates (dpm kg^{-1}[Ni]) as a function of the ^{53}Mn production rates (dpm kg^{-1}). The experimental data are shown by the solid black symbols. Also shown is the linear correlation predicted by the model calculations (gray band). Twenty of the available 23 experimental data follow the predicted linear trend; three irons (Benedict, Gan Gan, Turtle River) plot well above the correlation line. The meteorites Benedict and Turtle River have already been discussed before for their low ^{53}Mn data (see Fig. 5). Gan Gan has a very high ^{60}Fe production rate of 2.02 ± 0.37 dpm kg^{-1}(Ni), which indicates a rather small pre-atmospheric radius. Values that high are only possible close to the center of an iron meteorite with a pre-atmospheric radius in the range 20–30 cm (see Fig. 3). In such objects, however, the ^{53}Mn activities are in the range 550 dpm kg^{-1}, that is, far higher than the measured value of 323 ± 14 dpm kg^{-1}. The calculated pre-atmospheric radius in the range 20–30 cm is in reasonable agreement with the recovered mass of 83 kg, which corresponds to a post-atmospheric radius of ~13 cm. From these arguments, we speculate that the measured ^{53}Mn activity for Gan Gan is slightly too low.

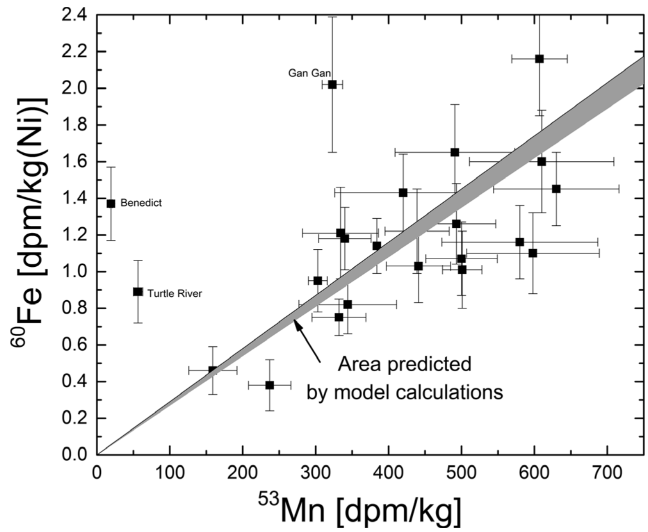

Fig. 6. Iron-60 production rates (dpm kg^{-1}[Ni]) as a function of ^{53}Mn production rates (dpm kg^{-1}). The experimental data are shown by solid black symbols. The gray shaded area indicates the linear correlation predicted by the new model calculations. Samples that deviate significantly from the predicted linear correlation are labeled.

CONCLUSIONS

We measured ^{53}Mn and ^{60}Fe activities in 41 and 28 iron meteorites, respectively, including six samples from the large iron meteorite Twannberg for ^{53}Mn. Measurements of ^{60}Fe and ^{53}Mn by accelerator mass spectrometry are both experimentally challenging. Consequently, prior to this study, the database for cosmogenic ^{53}Mn and for ^{60}Fe was limited to a few measurements only. In addition, we performed new model calculations for the production of ^{60}Fe and ^{53}Mn in iron meteorites. The model is based on the same particle spectra as a function of size and depth as used by Ammon et al. (2009), but our model uses only theoretical cross sections for proton- and neutron-induced reactions obtained from the INCL nuclear model code.

The new model predictions for ^{60}Fe are significantly higher than earlier ones and, with one exception (Grant; Berger et al. 2007), are in generally good agreement with the older and newer measurements for iron meteorites. There is still a discrepancy between measured and modeled ^{60}Fe data for the iron meteorite

Grant, which could well be due to inconsistent Grant data in a previous publication (Berger et al. 2007).

For ^{53}Mn, the new model predictions are on average 30% lower than the earlier model and are therefore in better agreement with experimental data. The new ^{53}Mn data for Grant are higher than the earlier data from Imamura et al. (1980) but are consistent with early AMS data (Merchel 1998) and are now in good agreement with the range predicted by the model for iron meteorites with a 40 cm pre-atmospheric radius. We found large variations among the ^{53}Mn activity concentrations of the six studied Twannberg samples, clearly confirming its exceptionally large pre-atmospheric size (Smith et al. 2017).

There are, however, still some discrepancies. Some of the measured ^{53}Mn/^{36}Cl and ^{60}Fe/^{53}Mn ratios do not fit into the allowed range in ^{53}Mn/^{36}Cl and do not follow the linear correlation between ^{60}Fe and ^{53}Mn predicted by our model, respectively. The discrepant data cannot be explained by complex exposure histories but might indicate some unrecognized problems either during sample preparation and/or during AMS measurements. The grand average of all measured data, however, agrees well with the average production rate ratio of ^{53}Mn/^{36}Cl ~31 and ^{60}Fe/^{53}Mn ~3.6×10^{-3} calculated with our model by considering all shielding depths in iron meteorites with pre-atmospheric radii between 5 and 120 cm.

In iron meteorites, ^{10}Be and ^{26}Al are often not very reliable due to possible contributions from traces of sulfur and/or phosphorous. For ^{26}Al, such contributions can be in the range of tens of percent, even in samples that were visually expected to be devoid of any inclusions (see Smith et al. 2019). In addition, ^{41}Ca is often very difficult to measure and is strongly affected by decay during terrestrial residence. Furthermore, ^{36}Cl is difficult to study because of the need for a dedicated chemistry laboratory for the chemical extraction and high risk of cross contamination, especially in the AMS ion source. Consequently, it might well be that ^{53}Mn and ^{60}Fe are more reliable cosmogenic radionuclides for studying cosmic ray exposure histories of iron meteorites. However, for ^{53}Mn to become reliable, there is a need to establish a consistent and well-documented standard, which ideally should not be from a meteorite.

The quality of the model calculations has improved considerably by using calculated data, instead of using experimental cross sections that are based on a few measurements only and that are sometimes inconsistent. While this clearly demonstrates the good quality currently achieved by nuclear model codes to calculate nuclear cross sections (at least for some target–product combinations), it also indicates that there is still a need for more and more reliable cross section measurements.

Acknowledgments—The authors would like to thank the following museums and research institutes for providing samples: The Ege University Observatory Research and Application Center, Turkey; The Vienna Natural History Museum, Austria; The Field Museum, Chicago, USA; The Department of Mineralogy and Petrology, Poznań, Poland; the Royal Ontario Museum, Toronto, Canada; The "Centre Européen de Recherche et d'Enseignement en Géosciences de l'Environnement" (CEREGE), Aix-en-Provence, France; The London Natural History Museum, London, England; The Senckenberg Natural History Museum, Frankfurt am Main, Germany. We would also like to thank H.-E. Jenni and P. Enderli for their tireless work in the noble gas laboratories. We thank R. Aniol for her help during sample preparation and S. Beutner for the ICP-MS measurements. We thank Stephen Tims and L. Keith Fifield for help during the AMS measurements at the ANU and J. Hirtz (CEA Saclay and University of Bern) for help calculating the cross sections. Finally, we thank the reviewers D. Cook and G. Herzog for helpful and constructive reviews which helped improving the paper. This work has been supported by the Swiss National Science Foundation (SNF 200021-159562) by the Australian Research Council, project numbers DP140100136, DP180100495, and DP180100496 and by the Group of Eight Australia–Germany Joint Research Co-operation Scheme.

Editorial Handling—Dr. A. J. Timothy Jull

REFERENCES

Ammon K., Masarik J., and Leya I. 2008. Noble gases in Grant and Carbo and the influence of S- and P- rich mineral inclusions on the ^{41}K–^{40}K dating system. *Meteoritics & Planetary Science* 43:685–699.

Ammon K., Masarik J., and Leya I. 2009. New model calculations for the production of cosmogenic nuclides in iron meteorites. *Meteoritics & Planetary Science* 44:485–503.

Berger E. L., Faestermann T., Herzog G. F., Knie K., Korschinek G., Leya I., and Serefiddin F. 2007. ^{60}Fe activities of Canyon Diablo, Grant, and Dorofeevka. *Meteoritics & Planetary Science* 42:A18.

Cook D. L., Smith T., Leya I., Hilton C. D., Walker R. J., and Schönbächler M. 2018. Excess ^{180}W in IIAB iron meteorites: Identification of cosmogenic, radiogenic, and nucleosynthetic components. *Earth and Planetary Science Letters* 503:29–36.

David J.-C., Boudard A., Cugnon J., Ghali S., Leray S., Mancusi D., and Zanini L. 2013. Modeling astatine production in liquid lead-bismuth spallation targets. *The European Physical Journal A* 49:29.

Fifield L. K., Tims S. G., Stone J. O., Argento D. C., and De Cesare M. 2013. Ultra-sensitive measurements of ^{36}Cl and ^{236}U at the Australian National University. *Nuclear Instruments and Methods in Physics Research B* 294:126–131.

Fimiani L., Cook D. L., Faestermann T., Gómez-Guzmán J. M., Hain K., Herzog G., Knie K., Korschink G., Ludwig P., Park J., Reedy R. C., and Rugel G. 2016. Interstellar ^{60}Fe on the surface of the moon. *Physical Review Letters* 116:154404.

Fitoussi C., Raisbeck G. M., Knie K., Korschinek G., Faestermann T., Goriely S., Lunney D., Poutivtsev M., Rugel G., Waelbroeck C., and Wallner A. 2008. Search for supernova-produced ^{60}Fe in marine sediment. *Physical Review Letters* 101:121101.

Furukawa M. 1973. Private communication (1973) to J. Tobailem, C.-H. de Lassus St. Genies, CEA-N-1466(3) (1975).

Gensho R., Takeuchi S., and Honda M. 1972. Detection of trace amounts of manganese isotopes by surface ionization method. *Mass Spectroscopy* 20:211–222.

Gensho R., Nitho O., Makino T., and Honda M. 1979. Some long-lived and stable nuclides produced by nuclear reactions. *Physics and Chemistry of the Earth* 11:11–18.

Gladkis L. G. 2006. Development of AMS techniques for ^{53}Mn und ^{236}U. PhD thesis, Australian National University, Canberra, Australia. https://doi.org/10.25911/5d5fc99066d6d

Goel P. S. and Honda M. 1965. Cosmic-ray-produced ^{60}Fe in Odessa meteorite. *Journal of Geophysical Research* 70:747–748.

Goldschmidt V. M. 1954. *Geochemistry* (Edited by A. Muir), Oxford: Clarendon Press.

Herpers U., Herr W., and Wölfle R. 1969. Evaluation of ^{53}Mn (n, γ) activation, ^{2}6Al and special trace elements in meteorites by γ-coincidence techniques. *Astrophysics and Space Science Library* 12:387.

Honda M. and Imamura M. 1971. Half life of ^{53}Mn. *Physical Review* C4:1182–1188.

Honda M., Shedlovsky J. P., and Arnold J. R. 1961. Radioactive species produced by cosmic rays in iron meteorites. *Geochimica et Cosmochimica Acta* 22:133–154.

Imamura M., Shima M., and Honda M. 1980. Radial distribution of spallogenic K, Ca, Ti, V, and Mn isotopes in iron meteorites. *Zeitschrift für Naturforschung* 35a:267–279.

Knie K., Korschinek G., Faestermann T., Wallner C., Scholten J., and Hillebrandt W. 1999a. Indication for supernova produced ^{60}Fe activity on Earth. *Physical Review Letters* 83:18–21.

Knie K., Merchel S., Korschinek G., Faestermann T., Herpers U., Gloris M., and Michel R. 1999b. AMS measurements and model calculations of iron-60 production rates in iron meteorites. *Meteoritics & Planetary Science* 34:729–734.

Knie K., Faestermann T., Korschinek G., Rugel G., Rühm W., and Wallner C. 2000. High-sensitivity AMS for heavy nuclides at the Munich Tandem accelerator. *Nuclear Instrument and Methods in Physics Research* B172:717–720.

Knie K., Korschinek G., Faestermann T., Dorfi E. A., Rugel G., and Wallner A. 2004. ^{60}Fe anomaly in a deep-sea manganese crust and implications for a nearby supernova source. *Physical Review Letters* 93:171103.

Koll D., Busser C., Faestermann T., Gómes-Guzmán J. M., Hain K., Kinast A., Korschinek G., Krieg D., Lebert M., Ludwig P., and Quinto F. 2019a. Recent developments for AMS at the Munich tandem accelerator. *Nuclear Instruments and Methods in Physics Research B* 438:180–183.

Koll D., Korschinek G., Faestermann T., Gómez-Guzmán J., Kipfstuhl S., Merchel S., and Welch J. M. 2019b. Interstellar ^{60}Fe in Antarctica. *Physical Review Letters* 123:072701.

Kumabe I., Ogata H., Komatuzaki T., Inoue N., Tomita S., Yamada Y., Yamaki T., and Matsumoto S. 1963. (p, alpha) reactions on the even nuclei Ni-58, Ni-60, and Fe-56. *Nuclear Physics* 46:437–453.

Kutschera W. 1984. Accelerator mass spectrometry and nuclear physics. *Nuclear Instruments and Methods in Physics Research* B17:377–384.

Kutschera W., Billquist P. J., Frekers D., Henning W., Jensen K. J., Xiuzeng M., Pardo R., Paul M., Rehm K. E., Smither R. K., Yntema J. L., and Mausner L. F. 1984. Half-life of ^{60}Fe. *Nuclear Instrument and Methods in Physics Research* B5:430–435.

Lavrukina A. K., Kuznetsova R. I., and El Satarova M. 1964. Rate of formation of radioactive isotopes in chondrites by cosmic ray reactions. *Geochemistry International* 1:1129–1136.

Leya I. and Michel R. 2011. Cross sections for neutron-induced reactions up to 1.6 GeV for target elements relevant for cosmochemical, geochemical, and technological applications. *Nuclear Instruments and Methods in Physics Research* B269:2487–2503.

Ludwig P., Bishop S., Egli R., Chernenko V., Deneva B., Faestermann T., Famulok N., Fimiani L., Gómez-Guzmán J. M., Hain K., Korschinek G., Hanzlik M., Merchel S., and Rugel G. 2016. Time-resolved 2-million-year-old supernova activity discovered in Earth's microfossile record. *Proceedings of the National Academy of Sciences of the United States of America* 113:9232–9237.

Mancusi D., Boudard A., Carbonell J., Cugnon J., David J.-C., and Leray S. 2015. Improving the description of proton-induced one-nucleon removal in intranuclear-cascade models. *Physical Review C* 91:034602.

Martschini M., Fifield L. K., Froehlich M. B., Leckenby G., Pavetich S., Tims S. G., Tranter B., and Wallner A. 2019. New and upgraded ionization chambers for AMS at the Australian National University. *Nuclear Instruments and Methods in Physics Research* B438:141–147.

Merchel S. 1998. Über die Wechselwirkung der kosmischen Strahlung mit extraterrestrischer Materie: Radiochemische Bestimmung der Produktionsraten von kosmogenen langlebigen Radionukliden in Meteoriten. PhD thesis, Universität zu Köln, Cologne, Germany.

Merchel S. and Herpers U. 1999. An update on radiochemical separation techniques for the determination of long-lived radionuclides via accelerator mass spectrometry. *Radiochemica Acta* 84:215–219.

Merchel S., Faestermann T., Herpers U., Knie K., Korschinek G., Leya I., Michel R., Rugel G., and Wallner C. 2000. Thin- and thick-target cross sections for the production of ^{53}Mn and ^{60}Fe. *Nuclear Instruments and Methods in Physics Research* B172:806–811.

Nishiizumi K. and Honda M. 2007. Cosmogenic ^{60}Fe in iron meteorites: Measurements by low-level counting. *Meteoritics & Planetary Science* 42:A118.

Nishiizumi K., Caffee M. W., Finkel R. C., and Arnold J. R. 1991. ^{10}Be and ^{53}Mn in non-Antarctic iron meteorites. *Meteoritics* 26:379.

Ostdiek K. M., Anderson T. S., Bauder W. K., Bowers M. R., Clark A. M., Collon P., Lu W. L., Nelson A. D., Robertson D., and Skulski M. 2017. Activity measurement of ^{60}Fe through the decay of ^{60m}Co and confirmation of its half-life. *Physical Review* C95:055809.

Ott U., Merchel S., Herrmann S., Pavetich S., Rugel G., Faestermann T., Fimiani L., Gomez-Guzman J. M., Hain K., Korschinek G., Ludwig P., D'Orazio M., and Folco L. 2014. Cosmic ray exposure and pre-atmospheric size of the Gebel Kamil iron meteorite. *Meteoritics & Planetary Science* 49:1365–1374.

Pedoux S. and Cugnon J. 2011. Extension of the Liège intranuclear cascade model at incident energies between 2 and 12 GeV. Aspects of pion production. *Nuclear Physics A* 866:16–36.

Perron C. 1976. Cross sections for the production of stable and long-lived nuclides by high energy spallation of iron; cosmic ray implications. *Physical Review* C14:1108–1120.

Roy J. and Kohman T. 1957. Iron 60. *Canadian Journal of Physics* 35:649–655.

Rugel G., Faestermann T., Knie K., Korschinek G., Poutivtsev M., Schumann D., Kivel N., Günther-Leopold I., Weinreich R., and Wohlmuther M. 2009. New measurements of the ^{60}Fe half-life. *Physical Review Letters* 103:072502.

Schumann D., Kivel N., and Dressler R. 2019. Production and characterization of ^{60}Fe standards for accelerator mass spectrometry. *PloSONE* 14:e0219039.

Shore B. W., Wall N. S., and Irvine J. W. 1961. Interactions of 7.5 MeV protons with copper and vanadium. *Physical Review* 123:276–283.

Smith T., Hofmann B. A., Leya I., Merchel S., Pavetich S., Rugel G., and Scharf A. 2017. The cosmic-ray exposure history of the Twannberg iron meteorite (IIG). *Meteoritics & Planetary Science* 52:2241–2257.

Smith T., Cook D. L., Merchel S., Pavetich S., Rugel G., Scharf A., and Leya I. 2019. The constancy of galactic cosmic rays as recorded by cosmogenic nuclides in iron meteorites. *Meteoritics & Planetary Science* 54:2951–2976.

Sugiura N. and Hoshino H. 2003. Mn-Cr chronology of five IIIAB iron meteorites. *Meteoritics & Planetary Science* 35:117–143.

Villagrasa-Canton C., Boudard A., Ducret J.-E., Fernandez B., Leray S., Volant C., Armbruster P., Enqvist T., Hammache F., Helariutta K., Juradoet B., Ricciardi M.-V., Schmidt K.-H., Sümmerer K., Vivès F., Yordanov O., Audouin L., Bacri C.-O., Ferrant L., Napolitani P., Rejmund F., Stephan C., Tassan-Got L., Benlliure J., Casarejos E., Fernandez-Ordoñez M., Pereira J., Czajkowski S., Karamanis D., Pravikoff M., George J. S., Mewaldt R. A., Yanasak N., Wiedenbeck M., Connell J. J., Faestermann T., Heinz A., and Junghans A. 2007. Spallation residues in the reaction ^{56}Fe + p at 0.3A, 0.5A, 0.75A, 1.0A, and 1.5A GeV. *Physical Review* C75:044603.

Wallner A., Bichler M., Buczak K., Dressler R., Fifield L. K., Schumann D., Sterba J. H., Tims S. G., Wallner G., and Kutschera W. 2015. Settling the half-life of ^{60}Fe: Fundamental for a versatile astrophysical chronometer. *Physical Review Letters* 114:041101.

Wallner A., Feige J., Kinoshita N., Paul M., Fifield L. K., Golser R., Honda M., Linnemann U., Matsuzaki H., Merchel S., Rugel G., Tims S. G., Steier P., Yamagata T., and Winkler S. R. 2016. Recent near-Earth supernovae probed by global deposition of interstellar radioactive ^{60}Fe. *Nature* 532:69–72.

Wallner A., Froehlich M. B., Hotchkis M. A. C., Kinoshita N., Paul M., Martschini M., Pavetich S., Tims S. G., Kivel N., Schumann D., Honda M., Matsuzaki H., and Yamagata T. 2019. ^{60}Fe and ^{24}4Pu reveal multiple nearby supernovae with low r-process yields, in review.